Hindawi
International Journal of Aerospace Engineering
Volume 2024, Article ID 9004308, 15 pages
https://doi.org/10.1155/2024/9004308

Research Article

A Novel Strategy for Hypersonic Vehicle With Complex Distributed No-Fly Zone Constraints

Tao Zhengxin[1,2] **and Zhang Shifeng**[1,2]

[1]*College of Aerospace Science and Engineering, National University of Defense Technology, Changsha 410073, China*
[2]*Hunan Provincial Key Laboratory of Aerospace Cross-Domain Flight Vehicle System and Control Technology, Department of Science and Technology of Hunan Province, Changsha 410073, China*

Correspondence should be addressed to Zhang Shifeng; shifeng@hotmail.com

Received 18 December 2023; Revised 29 February 2024; Accepted 13 April 2024; Published 16 May 2024

Academic Editor: Binbin Yan

Aiming at solving trajectory planning problem with complex distributed no-fly zone constraints, this paper proposed a novel obstacle avoidance strategy. For longitudinal motion, an angle of attack adjustment method is employed to adjust lift and design the angle of attack profile, while adjusting the bank angle for range and altitude correction to meet terminal constraints. For lateral motion, this paper developed enhanced attractive, repulsive, and velocity potential fields. Combined with the proposed repulsive force reconstruction method, this effectively resolves the overmaneuvering problem of traditional artificial potential field methods (APFMs) for vehicle. In order to avoid mismatched magnitudes of attractive and repulsive forces, a complementary no-fly zone avoidance strategy based on minimum turn radius is introduced, updating the bank angle command during no-fly zone avoidance. Simulation results indicate that the proposed strategy can address the avoidance of sudden threat, proving to be feasible and effective for handling complex distributed no-fly zone avoidance problems.

Keywords: artificial potential field; hypersonic vehicle; no-fly zone; trajectory planning

1. Introduction

High hypersonic aircraft technology is one of the commanding heights in the development of aerospace. With its unprecedented flight speeds, exceptional maneuverability, and potent destructive capabilities, hypersonic vehicle has far-reaching impacts on the development of military and technology [1].

The research on trajectory planning for hypersonic vehicles has consistently been a pivotal and prominent issue [2–4]. The trajectory of vehicle needs to satisfy multiple constraints, including dynamic pressure, heat flux density, terminal state requirements, and maneuverability. Constraints can be predefined before launch, such as waypoints and no-fly zones due to geographical obstacles, or they can be dynamically identified during flight, such as sudden threat areas detected by surveillance radars [5–7]. As the economy and society continue to develop, the increasing complexity in the number and distribution of no-fly zones poses a significant challenge to trajectory planning [8].

Scholars both domestically and internationally have shown significant interest in the trajectory planning of hypersonic vehicles under complex no-fly zone constraints. Current research on trajectory planning predominantly employs methods like pseudospectral methods [9], convex optimization [10], and heuristic algorithms [11], which incorporate constraints into the trajectory planning problem. The first two methods are known for their strong optimality and convergence properties. The outcomes derived from pseudospectral methods are notably sensitive to the selection of initial values [12], while convex optimization approaches may exhibit restricted efficacy when dealing with nonconvex constraints such as no-fly zones, necessitating the convexification of the problem [13]. Heuristic algorithms are well-suited for addressing global search problems but may exhibit reduced solution efficiency [14]. Researchers have refined these methodologies and obtained positive outcomes. Zhang et al. [15, 16] proposed a path-trajectory dual-level planning method for hypersonic vehicles under

complex no-fly zone constraints to avoid getting trapped in local solutions and reduce the error caused by simplifying the motion model. Chen et al. [17] introduced an iterative algorithm to estimate the switching position and re-entry flight time, aiming to guide the hypersonic vehicle to enter the midterminal guidance switch window successfully while adhering to no-fly zone constraints in scenarios where the target is undergoing rapid maneuvers. Tian et al. [18] employed pseudospectral methods to discretize control and state variables, thereby converting the re-entry trajectory planning problem into a nonlinear programming problem, and the optimization objective was to minimize heat flux and trajectory oscillations during the re-entry phase.

The artificial potential field method (APFM) is a renowned path planning method extensively employed in domains such as unmanned vehicles [19], drones [20, 21], and robotic arms [22] owing to its succinct mathematical formulation and rapid computational efficiency. However, it is prone to be susceptible to get stuck in local optima and may fail to reach the target point if the distance to obstacles is too close, or alternatively, it may lead to potential collisions when the distance is excessive. Hence, it is common practice to implement enhancements to this method. Ren et al. [23] proposed a potential function that effectively captures the geometric characteristics of objects with arbitrary shapes. Li et al. [24] formulated an adaptive stride corridor through the integration of guidance and no-fly zone avoidance strategies utilizing the repulsive force of the artificial potential field, followed by a comprehensive analysis of its convergence properties. Hu et al. [25] conducted a quantitative assessment of the threat posed by no-fly zones and developed an enhanced adaptive heading corridor guidance strategy by leveraging improved APFM. Hu et al. [26] proposed a dynamic heading corridor design algorithm based on improved APFM, which employs sliding mode control to follow a prescribed trajectory while simultaneously guaranteeing no-fly zone avoidance without diverting from the desired target point. Wang et al. [27] took multiple constraints into account and used a piecewise analytical polynomial height-velocity profile to deduce the analytical expression for commands of bank angle, and this methodology effectively utilizes the width of the entry corridor and effectively meets extensive range requirements in flight missions.

The aforementioned methods encounter certain challenges when confronted with intricate no-fly zones. The no-fly zone avoidance strategies employed by APFM tend to be conservative, which results in ineffective avoidance maneuvers during flight. Moreover, the formulation of an avoidance strategy is contingent upon initial conditions, leading to limited adaptability to cope with dynamic constraints such as changing no-fly zones during flight. Consequently, it is necessary to find an appropriate strategy that lets vehicle avoid the no-fly zones without excessive maneuvering and can meet the needs of multiple types of no-fly zones.

Motivated by the preceding discussion and with the objective of addressing solving trajectory planning problem with complex distributed no-fly zone constraints, this paper proposes a trajectory planning algorithm for complex distributed no-fly zone avoidance problems. For the lateral motion of vehicle, the lift is changed by adjusting the angle of attack, and the angle of attack profile is designed in a coordinated manner. To satisfy terminal constraints, the bank angle is modified to correct the range and altitude. In order to regulate the vehicle's lateral motion, an improved APFM is employed, which introduces improved attractive, repulsive, and velocity potential fields. Traditional APFM during flight always causes excessive maneuvering of vehicle during flight. To solve such problem, the avoidance strategy for lateral motion combined with repulsive force reconstruction is proposed to calculate the bank angle amplitude command, which can reduce the superposition of repulsive forces and decrease excessive maneuvering in flight. In order to avoid mismatched magnitudes of attractive and repulsive forces generated by APFM, a no-fly zone avoidance strategy based on minimum turning radius is proposed, which updates bank angle amplitude command when avoiding no-fly zones. The bank angle corridor is formulated to fulfill path constraints during flight. Simulation demonstrates the effectiveness of the proposed method, and the examples of sudden threat reflect the strong applicability of the method in addressing complex distributed no-fly zone avoidance challenges.

2. Dynamics Model and Constraints of Hypersonic Vehicle

Without considering the Earth's rotation, the dynamic model of the vehicle is shown:

$$\begin{cases} \dot{r} = V \sin\theta \\ \dot{\lambda} = \dfrac{V \cos\theta \sin\Psi}{r \cos\varphi} \\ \dot{\varphi} = \dfrac{V \cos\theta \cos\Psi}{r} \\ \dot{V} = -\dfrac{D}{m} - g \sin\theta \\ \dot{\theta} = \dfrac{1}{V}\left[\dfrac{L \cos\sigma}{m} + \left(\dfrac{V^2}{r} - g\right)\cos\theta\right] \\ \dot{\Psi} = \dfrac{1}{V}\left[\dfrac{L \sin\sigma}{m \cos\theta} + \dfrac{V^2 \cos\theta \sin\Psi \tan\varphi}{r}\right] \\ H = r - R_e \\ L = qS_rC_L \\ D = qS_rC_D \\ q = \dfrac{1}{2}\rho V^2 \end{cases} \tag{1}$$

where r is the geocentric distance, λ and φ are the longitude and the latitude, respectively, V is the velocity of vehicle, θ denotes the flight path angle, Ψ means the heading angle which is the angle between the projection of velocity on the local horizontal plane and the true north direction, σ

denotes the bank angle, g is the gravity acceleration, m is the vehicle's mass, H means the height of the vehicle, ρ is the atmospheric density at H, R_e is the Earth's radius, L and D are the aerodynamic lift and drag, C_L and C_D are the aerodynamic lift and drag, respectively, q denotes the dynamic pressure of vehicle, and S_r means the reference area of vehicle.

In this paper, the Common Aero Vehicle (CAV-H) is taken as the research object [28, 29]. References [30, 31] provide a method for fitting the aerodynamic coefficients of the CAV-H by using a binary quadratic polynomial model, which is expressed as follows:

$$\begin{cases} C_L = 0.11139 - 0.019871M + 4.161 \times 10^{-4}M^2 + 2.2991\alpha + 1.2292\alpha^2 \\ C_D = 0.23462 - 0.02421M + 7.089 \times 10^{-4}M^2 - 0.17481\alpha + 2.7251\alpha^2 \end{cases} \tag{2}$$

where M is the number and α is the angle of attack.

Considering the limited control capability of the vehicle, constraints are imposed on the bank angle and the rate of change of the bank angle.

$$|\sigma| \leqslant \sigma_{\max}, |\dot{\sigma}| \leqslant \dot{\sigma}_{\max} \tag{3}$$

In the formula, $\sigma_{\max}$ is the maximum bank angle, and $\dot{\sigma}_{\max}$ is the maximum rate of change of the bank angle.

In addition to the dynamic constraints, the vehicle must also satisfy the constraints of dynamic pressure $q_{\max}$, heat flux density $\dot{Q}_{\max}$, and load factor $n_{\max}$, which can be expressed as

$$\begin{cases} \dot{Q} = k_Q \sqrt{\rho} V^3 \leqslant \dot{Q}_{\max} \\ n = \dfrac{q\sqrt{C_L^2 + C_D^2} S_r}{mg} \leqslant n_{\max} \\ q = \dfrac{gR_e \rho V^2}{2} \leqslant q_{\max} \end{cases} \tag{4}$$

In this paper, no-fly zones are defined as circular areas that vehicles are not allowed to pass through and can be represented as

$$\sqrt{(\lambda_o - \lambda)^2 + (\varphi_o - \varphi)^2} \geqslant R_o \tag{5}$$

where λ_o and φ_o represent the longitude and latitude of the center of the no-fly zone, respectively, and R_o denotes the radius of the no-fly zone.

3. Obstacle Avoidance Strategy

To avoid the no-fly zones, this paper proposes a trajectory planning algorithm based on improved APFM. When traditional APFM is used for trajectory planning, the trackability of the trajectory is usually not considered, and only geometrically feasible trajectories are obtained. However, the vehicle is limited by its own maneuvering capability and cannot track arbitrarily shaped geometric trajectories. Therefore, in the trajectory planning stage, this paper combines the vehicle's dynamic model and constraints to design an avoidance strategy.

3.1. Strategy for Longitudinal Motion. To compensate for the altitude loss during the avoidance of no-fly zones, this paper adjusts lift by adjusting the angle of attack. The vehicle typically needs to satisfy the *quasiequilibrium gliding condition* (QEGC) during flight.

$$L \cos \sigma = m\left(g - \frac{V^2}{r}\right) \tag{6}$$

The required lift L can be calculated, and the required angle of attack α can be obtained through the method of aerodynamic coefficient difference.

$$C_L(\alpha) = \frac{2L}{\rho V^2 S_r} \tag{7}$$

A large bank angle will lead to significant speed loss when compensating for altitude loss since the required angle of attack is large. Therefore, it is necessary to design a reasonable range to adjust the angle of attack $[\alpha_{\text{low}}, \alpha_{\max}]$.

Considering that the vehicle needs to meet the process constraints, the attack angle profile is designed as the function of velocity.

$$\alpha = \begin{cases} \alpha_m, V > V_m \\ \dfrac{\alpha_{L/D} - \alpha_m}{V_{L/D} - V_m}(V - V_{\text{m}}) + \alpha_m, V_{L/D} \leqslant V \leqslant V_m \\ \alpha_{L/D}, V \leqslant V_{L/D} \end{cases} \tag{8}$$

In the formula, α_m is the max angle of attack limited by the aerodynamic, $\alpha_{L/D}$ is the best angle of attack when the ratio of lift to drag takes the maximum value, and $V_{L/D}$ and V_m are the design variables, which control the angle of attack for different flight phases.

In order to ensure a stable flight before the vehicle reaches equilibrium, set the bank angle to 0 when the velocity exceeds the design velocity.

$$\sigma = 0, V > V_m \tag{9}$$

To meet the constraints on terminal altitude, a design flight path angle feedback control strategy is designed to adjust the angle of attack. The desired flight path angle θ_d can be expressed as

$$\theta_d = \operatorname{atan} \frac{s}{h_0 - h_f} \tag{10}$$

where h_0 is the initial altitude of the vehicle, h_f means the terminal altitude of the vehicle, s denotes the rest of the range which can be calculated from the current position of the vehicle and the target point's latitude and longitude.

The linear feedback tracking control law is designed as

$$\dot{\theta}_d = -k_\theta |\theta - \theta_d| \tag{11}$$

According to Equation (11), the required lift L' can be calculated:

$$L' = \frac{m}{\cos\sigma}\left[V\dot{\theta}_d + \left(g - \frac{V^2}{r}\right)\cos\theta\right] \tag{12}$$

The required angle of attack α' can be obtained through the method of aerodynamic coefficient difference.

$$C_L\left(\alpha'\right) = \frac{2L'}{\rho V^2 S_r} \tag{13}$$

After avoiding no-fly zones, the vehicle will experience corresponding losses in altitude and speed. In order to meet the terminal constraints, corrections need to be made to the flight distance and altitude. In this paper, the adjustment of the bank angle is used to achieve the correction of the flight distance. The energy calculation formula is defined as

$$e = \frac{1}{2}\left(\frac{V}{V_c}\right)^2 - \frac{R_e}{r} \tag{14}$$

In the formula, $V_c = \sqrt{gR_e}$.

According to reference [32], an energy-based motion model is derived for flight distance prediction.

$$s_{\text{pre}} = \frac{1}{2}\frac{L}{D}\cos\sigma \ln\left(\frac{2re_f - 1}{2re - 1}\right) \tag{15}$$

where in $\Delta s = s - s_{\text{pre}}$, s_{pre} means the projection of the remaining range, and e_f is the energy value at the end time.

The online correction of range is achieved by adjusting the bank angle, which uses the secant method for iterative calculation of the bank angle value.

$$|\sigma(\tau+1)| = |\sigma(\tau)| - \frac{|\sigma(\tau)| - |\sigma(\tau-1)|}{\Delta s_\tau - \Delta s_{\tau-1}}\Delta s_\tau \tag{16}$$

where subscript τ is the number of iterations; the iterations end when $||\sigma(\tau+1)| - |\sigma(\tau)|| < \varepsilon$, and ε is a given small number. By using this method, the error in flight distance can be suppressed effectively.

3.2. Avoidance Strategy for Lateral Motion. To control the lateral movement of vehicle, a strategy needs to be used to compute the appropriate magnitude of the bank angle for effectively tracking the reference profile, and such strategy is adopted to specify the sign of bank angle for eliminating heading errors. In this paper, besides the above discussion, the ability to avoid no-fly zones is also taken into consideration when designing the strategy. In this section, the lateral motion of vehicle is determined by APFM, and to avoid mismatched magnitudes of attractive and repulsive forces, a complementary avoidance strategy based on minimum turn radius is introduced when the vehicle is close to the obstacle.

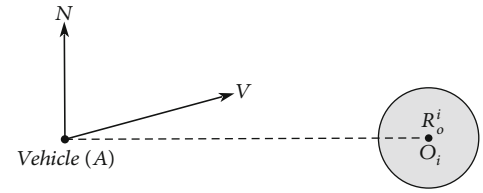

Figure 1: Avoidance based on APFM.

3.2.1. Avoidance Strategy Based on Improved APFM. As shown in Figure 1, the position of the vehicle is denoted as A, and the line connecting the vehicle and the center of ith no-fly zone O_i is $\overline{O_iA}$. If the vehicle is not close to the no-fly zone ($||\overline{O_iA}|| > K_{vo}R_o^i$, K_{vo} is distance factor), the improved APFM is employed to determine lateral motion. The force generated by improved APFM can be divided into attractive force and repulsive force. The magnitude of attractive force is related to the relative position of the aircraft and the no-fly zones. The magnitude of repulsive force is dictated by the relative position and relative speed of the aircraft and the no-fly zones. The resultant force of attractive and repulsive forces determines the command bank angle of the vehicle.

3.2.1.1. Design of Attractive Potential Field. The attractive potential function of the target is designed as

$$U_{\text{att}} = \begin{cases} \dfrac{1}{2}K_a d^2\left(\boldsymbol{p}, \boldsymbol{p}_{\text{goal}}\right), d\left(\boldsymbol{p}, \boldsymbol{p}_{\text{goal}}\right) \leqslant d_{\text{thres}} \\ K_a d\left(\boldsymbol{p}, \boldsymbol{p}_{\text{goal}}\right) d_{\text{thres}} - \dfrac{1}{2}K_a d_{\text{thres}}^2, \text{others} \end{cases} \tag{17}$$

In the formula, K_a is the attractive coefficient, $\boldsymbol{p} = (\lambda, \varphi)$ means the current longitude and latitude of vehicle, $\boldsymbol{p}_{\text{goal}} = (\lambda_{\text{goal}}, \varphi_{\text{goal}})$ denotes the longitude and latitude of target, $d(\boldsymbol{p}, \boldsymbol{p}_{\text{goal}})$ is the geodesic distance between the current position of the vehicle and the target, and d_{thres} means the threshold distance between the vehicle and the target.

The force of attraction is the negative gradient of the attractive potential field and can be expressed as

$$F_{\text{att}} = \nabla U_{\text{att}} = \begin{cases} K_a\left(\boldsymbol{p} - \boldsymbol{p}_{\text{goal}}\right), d\left(\boldsymbol{p}, \boldsymbol{p}_{\text{goal}}\right) \leqslant d_{\text{thres}} \\ \dfrac{K_a d_{\text{thres}}\left(\boldsymbol{p} - \boldsymbol{p}_{\text{goal}}\right)}{d\left(\boldsymbol{p}, \boldsymbol{p}_{\text{goal}}\right)}, \text{others} \end{cases} \tag{18}$$

In this attractive field, when $d(\boldsymbol{p}, \boldsymbol{p}_{\text{goal}}) \leqslant d_{\text{thres}}$, the force of attraction experienced by the vehicle is positively correlated with distance between the vehicle and the target, and when $d(\boldsymbol{p}, \boldsymbol{p}_{\text{goal}}) > d_{\text{thres}}$, the force of attraction experienced by the vehicle is negatively correlated with distance between the vehicle and the target. It can prevent the issue of the vehicle failing to avoid no-fly zones due to excessive attractive force resulting from large distances.

3.2.1.2. Design of Repulsive Potential Field. The repulsive potential function is designed as

$$U_{\text{rep}}^{i} = \begin{cases} 0, d\left(\boldsymbol{p}, \boldsymbol{p}_o^i\right) > K_o R_o^i \\ \dfrac{1}{2} K_r \left(\dfrac{1}{d(\boldsymbol{p}, \boldsymbol{p}_o^i)} - \dfrac{1}{K_o R_o^i}\right)^2 d^{n_0}\left(\boldsymbol{p}, \boldsymbol{p}_o^i\right), \text{others} \end{cases} \tag{19}$$

where K_r is the repulsive coefficient, n_0 denotes the correction coefficient, $\boldsymbol{p}_o^i = (\lambda_o^i, \varphi_o^i)$ means the longitude and latitude of the center of ith no-fly zone, R_o^i is the radius, $d(\boldsymbol{p}, \boldsymbol{p}_o^i)$ denotes the geodesic distance from the current location of the vehicle and the center of ith no-fly zone, and K_o is the effective repulsive factor which describes the effective range of repulsion for no-fly zones.

The force of repulsion, which is the negative gradient of the repulsive potential field, is denoted as

$$F_{\text{rep}}^{i} = \nabla U_{\text{rep}}^{i} = \begin{cases} F_{\text{rep}(1)}^{i} + F_{\text{rep}(2)}^{i}, d\left(\boldsymbol{p}, \boldsymbol{p}_o^i\right) \leqslant K_o R_o^i \\ 0, d\left(\boldsymbol{p}, \boldsymbol{p}_o^i\right) > K_o R_o^i \end{cases} \tag{20}$$

$$F_{\text{rep}(1)}^{i} = -\frac{n_0 K_r}{2} \left(\frac{1}{d(\boldsymbol{p}, \boldsymbol{p}_o^i)} - \frac{1}{K_o R_o^i}\right)^2 d^{n_0 - 1}\left(\boldsymbol{p}, \boldsymbol{p}_{\text{goal}}\right) \tag{21}$$

$$F_{\text{rep}(2)}^{i} = K_r \left(\frac{1}{d(\boldsymbol{p}, \boldsymbol{p}_o^i)} - \frac{1}{K_o R_o^i}\right) \frac{d^{n_0}\left(\boldsymbol{p}, \boldsymbol{p}_{\text{goal}}\right)}{d^2(\boldsymbol{p}, \boldsymbol{p}_o^i)} \tag{22}$$

The repulsive function has been improved by introducing a correction coefficient $d^{n_0}(\boldsymbol{p}, \boldsymbol{p}_o^i)$, which avoids situations where the vehicle deviates from the target due to excessive repulsion when the vehicle is close to a no-fly zone. The repulsive function also combines the effective range of repulsion with the radius of the no-fly zone, enhancing its adaptability to different no-fly zones.

When the jth no-fly zone is moving, the velocity repulsive potential function $U_{\text{rep}v}^{j}$ can be designed to enable the vehicle to have the ability to avoid the moving no-fly zone.

$$U_{\text{rep}v}^{j} = \begin{cases} K_{rv} V_{\text{rel}} \sin \eta_{\text{rel}}, d\left(\boldsymbol{p}, \boldsymbol{p}_o^j\right) \leqslant K_o R_o^j \\ 0, d\left(\boldsymbol{p}, \boldsymbol{p}_o^j\right) > K_o R_o^j \end{cases} \tag{23}$$

In the formula, K_{rv} is the velocity repulsive coefficient, V_{rel} means the velocity of the vehicle relative to the jth no-fly zone, and η_{rel} represents the angle between the position vector of the vehicle relative to the center of the jth no-fly zone and V_{rel}.

The force of velocity, which is the negative gradient of the velocity repulsive potential field, is expressed as

$$F_{\text{rep}v}^{j} = \nabla U_{\text{rep}v}^{j} = \begin{cases} \dfrac{K_{rv} V_{\text{rel}}}{d\left(\boldsymbol{p}, \boldsymbol{p}_o^j\right)}, d\left(\boldsymbol{p}, \boldsymbol{p}_o^j\right) \leqslant K_o R_o^j \\ 0, d\left(\boldsymbol{p}, \boldsymbol{p}_o^j\right) > K_o R_o^j \end{cases} \tag{24}$$

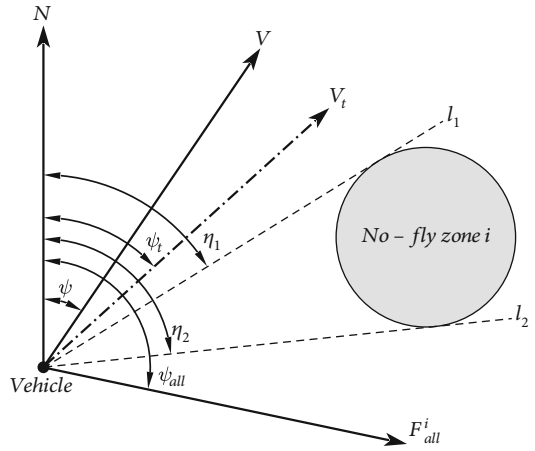

Figure 2: Collision prediction based on velocity and force.

The repulsive function of jth no-fly zone is updated as follows:

$$F_{\text{rep}}^{j} = F_{\text{rep}O}^{j} + F_{\text{rep}v}^{j} \tag{25}$$

where $F_{\text{rep}O}^{j}$ means the repulsive force calculation without considering the movement of the no-fly zone.

The resultant repulsive force is the sum of repulsive force from each no-fly zone acting on the vehicle.

$$F_{\text{rep}} = \sum_{i=1}^{N} F_{\text{rep}}^{i} \tag{26}$$

In the formula, N means the number of no-fly zones.

3.2.2. Repulsive Force Reconstruction. The resultant force acting on the vehicle under attractive and repulsive potential fields is denoted as F_{all}.

$$F_{\text{all}} = F_{\text{att}} + F_{\text{rep}} \tag{27}$$

The APFM may produce invalid maneuvers for no-fly zones that are not on the flight path of the vehicle. Many scholars have proposed collision prediction methods to avoid invalid maneuvers, but most of them are similar to the method in reference [33], which only uses the flight direction and relative position of the vehicle to the no-fly zone as prediction conditions, ignoring the resultant force acting on the vehicle.

This paper incorporates the resultant force into collision prediction. As shown in Figure 2, assuming that the repulsive force from ith no-fly zone is not considered, the resultant force acting on the vehicle is

$$F_{\text{all}}^{i} = F_{\text{all}} - F_{\text{rep}}^{i} \tag{28}$$

The angle between F_{all}^{i} and the north direction is denoted as ψ_{all}, the tangents to the boundaries of the ith no-fly zone from the vehicle are represented by l_1 and l_2,

the angles between tangent and the north direction are η_1 and η_2, respectively ($\eta_1 \leqslant \eta_2$), and ψ_t means the angle between the direction of V and the north direction at time t. Under the influence of F^i_{all}, ψ_{all} satisfies the following relationship:

$$\begin{cases} \psi_{\text{all}} \leqslant \psi_t \leqslant \psi, \psi_{\text{all}} \leqslant \psi \\ \psi \leqslant \psi_t \leqslant \psi_{\text{all}}, \psi \leqslant \psi_{\text{all}} \end{cases} \tag{29}$$

If the vehicle fails to avoid the no-fly zone, the direction of the velocity will point towards the no-fly zone at some point.

$$\eta_1 \leqslant \psi_t \leqslant \eta_2 \tag{30}$$

If there is no intersection between the range of ψ_t in Equation (29) and Equation (30), it indicates that the vehicle will not enter the no-fly zone under the influence of the resultant force; thus, there is no need to consider the repulsive force generated by a no-fly zone, and F^i_{rep} is assigned a value of 0. Based on the above discussion, the sufficient condition for the vehicle to disregard the repulsive force of the no-fly zone is expressed as

$$\begin{cases} [\psi_{\text{all}}, \psi] \cap [\eta_1 \eta_2] = \varnothing, \psi_{\text{all}} \leqslant \psi \\ [\psi, \psi_{\text{all}}] \cap [\eta_1 \eta_2] = \varnothing, \psi_{\text{all}} > \psi \end{cases} \tag{31}$$

If Equation (31) is not satisfied, it indicates that the vehicle may enter the no-fly zone, so the repulsive force generated by the no-fly zone should be considered.

The traditional APFM often sums up all the repulsive forces to calculate the resultant force, leading to a cumulative effect of repulsion that causes excessive maneuvering of the vehicle. To mitigate this impact, this paper decomposes the repulsive force to reduce its cumulative effect. As shown in Figure 3, this study assumes that the repulsive force $F^{1\sim k}_{\text{rep}}$ is on one side of the velocity V, and the repulsive force $F^{k+1\sim N}_{\text{rep}}$ is on the other side. The repulsive force generated by ith no-fly zone is projected along the tangent and normal directions of velocity, denoted as F^i_r and F^i_v, respectively. For $F^{1\sim k}_{\text{rep}}$, it is decomposed into sets $\boldsymbol{F}^{1\sim k}_r$ and $\boldsymbol{F}^{1\sim k}_v$.

$$\boldsymbol{F}^{1\sim k}_r = \left\{ F^1_r, F^2_r, \cdots, F^k_r \right\} \boldsymbol{F}^{1\sim k}_v = \left\{ F^1_v, F^2_v, \cdots, F^k_v \right\} \tag{32}$$

The repulsive force with the maximum scalar value from sets $\boldsymbol{F}^{1\sim k}_r$ and $\boldsymbol{F}^{1\sim k}_v$ is denoted as $F^{1\sim k}_{r\,\max}$ and $F^{1\sim k}_{v\,\max}$, respectively. It is evident that the resultant force of $F^{1\sim k}_{r\,\max}$ satisfies the avoidance requirements of all the no-fly zones corresponding to the repulsive forces in $F^{1\sim k}_{\text{rep}}$. Similarly, $F^{k+1\sim N}_{r\,\max}$ and $F^{k+1\sim N}_{v\,\max}$ can be calculated. Therefore, the resultant repulsive force of repulsive force reconstruction is expressed as

$$F_{\text{rep}} = \left(F^{1\sim k}_{r\,\max} + F^{k+1\sim N}_{r\,\max} \right) + \left(F^{1\sim k}_{v\,\max} + F^{k+1\sim N}_{v\,\max} \right) \tag{33}$$

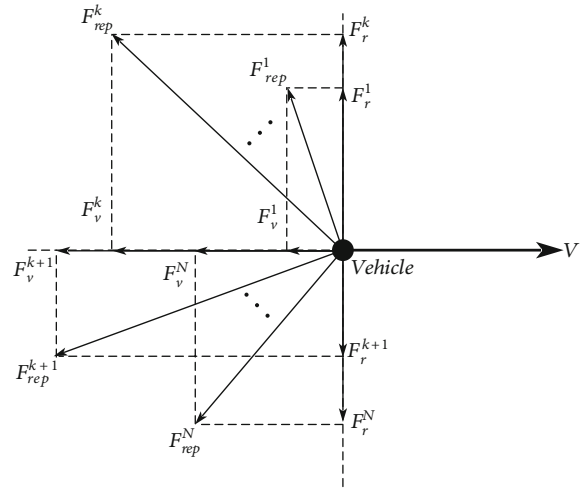

Figure 3: Decompose of repulsion force.

According to Equations (18) and (33), the resultant force F_{all} is recalculated. The reference heading angle ψ^* of the vehicle is the angle between the direction of F_{all} and the north direction. In this paper, the command bank angle σ_{cmd} is generated by resultant force F_{all}.

$$\sigma_{\text{cmd}} = K_\sigma \frac{F^\lambda_{\text{all}}}{\| F_{\text{all}} \|} \tag{34}$$

where F^λ_{all} is the projection of F_{all} along the longitude direction and K_σ represents the adjustment factor of command.

3.2.3. Avoidance Strategy Based on Minimum Turning Radius. The effectiveness of the APFM is highly dependent on the design parameters. When the vehicle is close to the obstacle, there is a risk of avoidance failure due to mismatched magnitudes of attractive and repulsive forces if parameters are designed unreasonably. To ensure successful avoidance, this paper proposes a strategy based on the minimum turning radius.

As shown in Figure 4, the angle between the $\overline{O_iA}$ and the north direction is denoted as η_0. If the vehicle is close to the no-fly zone ($\| \overline{O_iA} \| \leqslant K_{vo} R^i_o$) at time t, the turn must be executed to avoid the no-fly zone. R_v means the turning radius, and O_v represents the center of turning. The angle between $\overline{O_vA}$ and $\overline{O_iA}$ is denoted as δ_θ.

For ease of calculation, assuming that the turning radius remains constant during the flight. After a period of time Δt, the vehicle moves to A' where the velocity direction is perpendicular to $\overline{O_iA'}$. If AA' does not intersect with the no-fly zone, the vehicle has the ability to avoid the no-fly zone at time t, and the following relationship holds

$$\left\| \overline{O_vO_i} \right\| \geqslant R_v + R^i_o \tag{35}$$

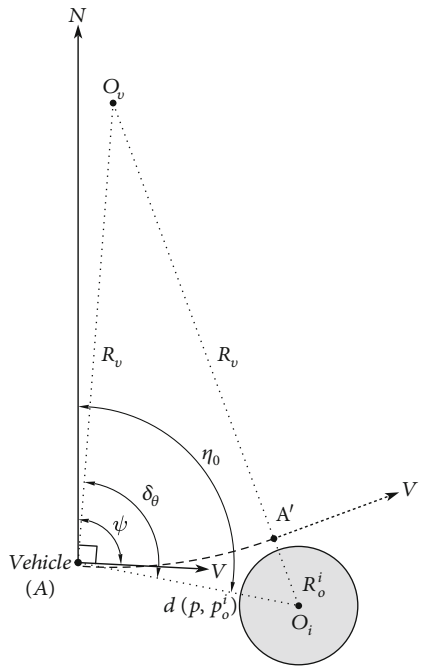

Figure 4: Avoidance based on minimum turning radius.

Based on geometric relationships, $\|\overline{O_vO_i}\|$ is expressed as

$$\begin{aligned}\left\|\overline{O_vO_i}\right\| &= \sqrt{\left\|\overline{O_iA}\right\|^2 + \left\|\overline{O_vA}\right\|^2 - 2\left\|\overline{O_iA}\right\|\left\|\overline{O_vA}\right\| \cos\delta_\theta} \\ &= \sqrt{{R_v}^2 + d^2\left(\boldsymbol{p}, \boldsymbol{p}_0^i\right) - 2R_v d\left(\boldsymbol{p}, \boldsymbol{p}_0^i\right) \cos\delta_\theta}\end{aligned} \tag{36}$$

Then, combine Equation (35) and Equation (36), which lead to

$$\frac{d^2\left(\boldsymbol{p}, \boldsymbol{p}_0^i\right) - \left(R_o^i\right)^2}{2} \geqslant \left(R_o^i - d\left(\boldsymbol{p}, \boldsymbol{p}_0^i\right) \sin\delta_\theta\right) R_v \tag{37}$$

If $(R_o^i - d(\boldsymbol{p}, \boldsymbol{p}_0^i) \sin\delta_\theta) \leqslant 0$, Equation (37) holds true, and the velocity direction of vehicle does not point towards the no-fly zone, so there is no need to make a maneuver, $\sigma_{\text{cmd}} = 0$.

If $(R_o^i - d(\boldsymbol{p}, \boldsymbol{p}_0^i) \sin\delta_\theta) > 0$, Equation (37) can be transformed as

$$R_v \leqslant \frac{d^2\left(\boldsymbol{p}, \boldsymbol{p}_0^i\right) - \left(R_o^i\right)^2}{2\left(R_o^i - d\left(\boldsymbol{p}, \boldsymbol{p}_0^i\right) \sin\delta_\theta\right)} \tag{38}$$

For BTT vehicle, the turning process is achieved by generating a lateral component of lift through the use of banked wings. This provides the required centripetal force for turning. Assuming that the vehicle is in QEGC with no side slip during the turning process, then the flight path angle is approximately zero.

During the turning process, the required centripetal force is provided by the lateral component of lift $L \sin\sigma$; thus, the turning radius R_v satisfies the following equation:

$$\frac{V^2}{R_v} = \frac{L \sin\sigma}{m} \tag{39}$$

Then, combine the $\dot{\theta}$ in Equation (1) and Equation (39), which lead to

$$R_v = \frac{V^2}{\tan\sigma\left(g - \left(V^2/r\right)\right)\cos\theta} \tag{40}$$

By neglecting the centrifugal force within the horizontal turning plane, an approximate solution for the turning radius can be obtained as follows

$$R_v = \frac{V^2}{g \tan\sigma} \tag{41}$$

Replacing R_v in Equation (38) and Equation (41), the range of bank angle can be expressed as

$$\tan\sigma \geqslant \frac{2V^2\left(R_o^i - d\left(\boldsymbol{p}, \boldsymbol{p}_0^i\right) \sin\delta_\theta\right)}{g\left(d^2\left(\boldsymbol{p}, \boldsymbol{p}_0^i\right) - \left(R_o^i\right)^2\right)} \tag{42}$$

In this study, when $(R_o^i - d(\boldsymbol{p}, \boldsymbol{p}_0^i) \sin\delta_\theta) > 0$, the command bank angle σ_{cmd} is valued as

$$\sigma_{\text{cmd}} = \operatorname{atan}\left(\frac{2V^2\left(R_o^i - d\left(\boldsymbol{p}, \boldsymbol{p}_0^i\right) \sin\delta_\theta\right)}{g\left(d^2\left(\boldsymbol{p}, \boldsymbol{p}_0^i\right) - \left(R_o^i\right)^2\right)}\right) \tag{43}$$

When using the avoidance strategy based on the minimum turning radius, the vehicle's reference heading angle ψ^* remains consistent with its actual heading angle ψ, which means $\psi^* = \psi$.

3.3. Bank Angle Corridor Design. During the flight process, the vehicle needs to satisfy constraints related to dynamic pressure $q_{\max}$, heat flux density $\dot{Q}_{\max}$, and aerodynamic load $n_{\max}$. Reference [34] provides a representation of these constraints using bank angle as a variable.

$$\cos\sigma_{\max\, q} \geqslant \frac{gR_e\left(1 - V^2\right)}{2K_L q_{\max}} \tag{44}$$

$$\cos\sigma_{\max\, \dot{Q}} \geqslant \frac{k_Q^2 V^4\left(1 - V^2\right)}{K_L \dot{Q}_{\max}} \tag{45}$$

$$\cos\sigma_{\max\, n_{\max}} \geqslant \frac{\left(1 - V^2\right)}{n_{\max}}\left(\cos\alpha + \frac{C_D}{C_L}\sin\alpha\right) \tag{46}$$

where $\sigma_{\max\, q}$ represents the maximum bank angle under the constraint of dynamic pressure, $\sigma_{\max\, \dot{Q}}$ is the maximum bank angle under the constraint of heat flux density, and $\sigma_{\max\, n_{\max}}$ means the maximum bank angle under the constraint of aerodynamic load, $k_Q = 9.43692(\sqrt{gR_e})^3$ and $K_L = R_e S_r C_L / 2m$.

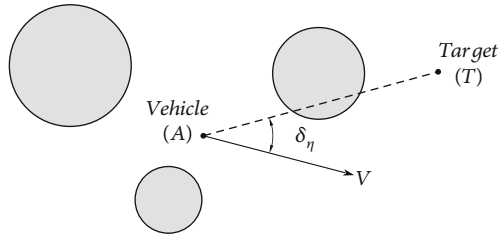

Figure 5: Vehicle avoids part of no-fly zones.

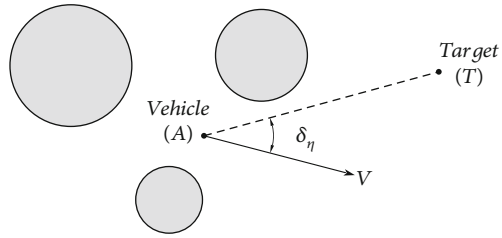

Figure 6: Vehicle avoids all no-fly zones.

Define the smallest upper bound of allowable bank angle magnitude by

$$\sigma_{\text{cmd}} \leqslant \min\left\{\sigma_{\max\, q}, \sigma_{\max\, \dot{Q}}, \sigma_{\max\, n_{\max}}, \sigma_{\max}\right\} \tag{47}$$

The reversal logic of the bank angle is employed to govern the sign. The heading angle error threshold is denoted as $\delta\psi$, and the reference heading corridor is obtained.

$$\begin{cases} \psi_{\text{up}} = \psi^* + \delta\psi \\ \psi_{\text{down}} = \psi^* - \delta\psi \end{cases} \tag{48}$$

When the heading angle exceeds the corridor, change the sign of the bank angle; otherwise, keep the sign of the bank angle unchanged.

$$\text{sign}\left(\sigma^n_{\text{cmd}}\right) = \begin{cases} -1 \psi > \psi_{\text{up}} \\ 1 \psi < \psi_{\text{down}} \\ \text{sign}\left(\sigma^{n-1}_{\text{cmd}}\right) \text{others} \end{cases} \tag{49}$$

where σ^n_{cmd} is the command bank angle in the current calculation cycle and $\sigma^{n-1}_{\text{cmd}}$ means the command bank angle in the previous calculation cycle.

3.4. Terminal Guidance Algorithm Design. As shown in Figures 5 and 6, the position of vehicle is denoted as A, the position of target is denoted as T, and the angle between the vehicle's velocity vector and the line $\overline{\text{AT}}$ is denoted as δ_η.

If $\overline{\text{AT}}$ intersect with no-fly zones (Figure 5), the vehicle has not avoided all obstacles. If there is no intersection (Figure 6), the vehicle is considered to have avoided all obstacles, and adjusting the command bank angle magnitude to align the vehicle's flight direction with the target point.

$$\sigma_{\text{cmd}} = K_{\text{ad}} \sigma_{\text{cmd}O} \tag{50}$$

where K_{ad} is the adjusting factor and $\sigma_{\text{cmd}O}$ denotes the original command bank angle before adjustment.

If the deviation between the vehicle's motion direction and $\overline{\text{AT}}$ is small, the vehicle is considered to be aligned with the target, then set σ_{cmd} to 0 until the vehicle reaches the target.

$$\sigma_{\text{cmd}} = 0, \left|\delta_\eta\right| \leqslant \delta_{\min} \tag{51}$$

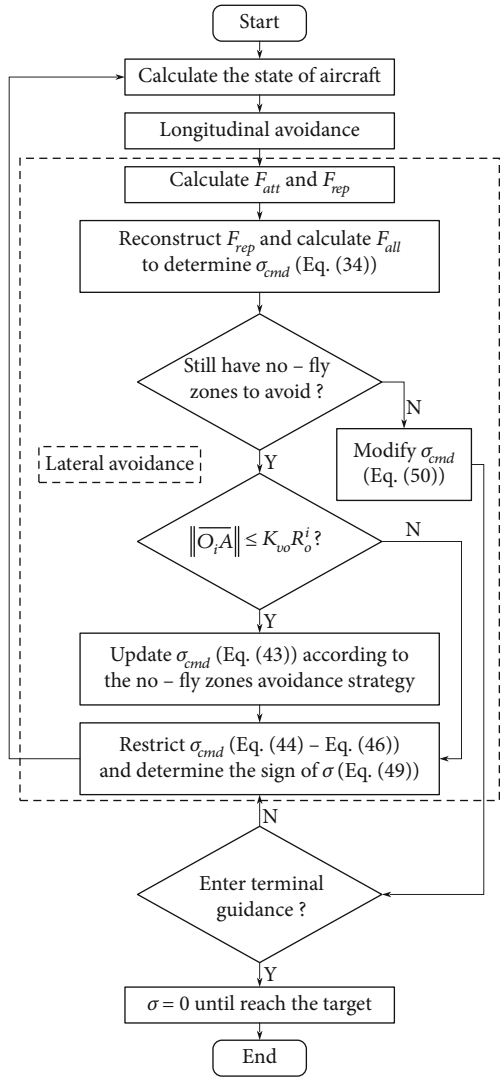

Figure 7: Flowchart of proposed avoidance strategy.

Table 1: Parameters of the proposed strategy.

Parameter	Value	Parameter	Value
K_a	57.3	K_{rv}	0.0052
d_{thres}/km	2774	K_{vo}	3
K_r	0.2618	K_{ad}	2
K_o	10	$\delta_{\min}/^\circ$	0.1
n_0	2		

Table 2: Information of no-fly zones.

No-fly zone	Position		Radius/km
	Lon/°	Lat/°	
1	30	10	500
2	36	-9	600
3	55	5	500
4	58	-6	400
5	80	0	500

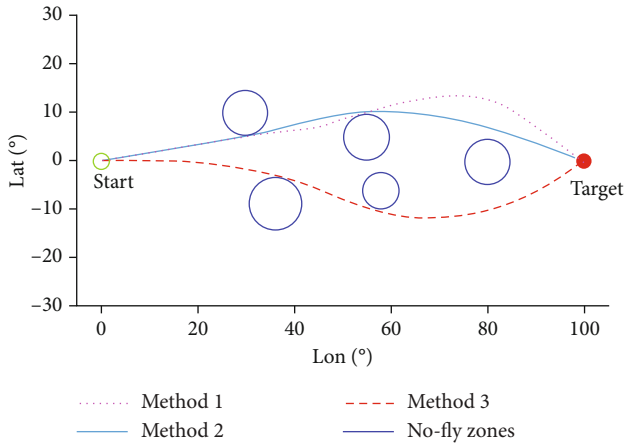

Figure 8: Ground track comparison of vehicle.

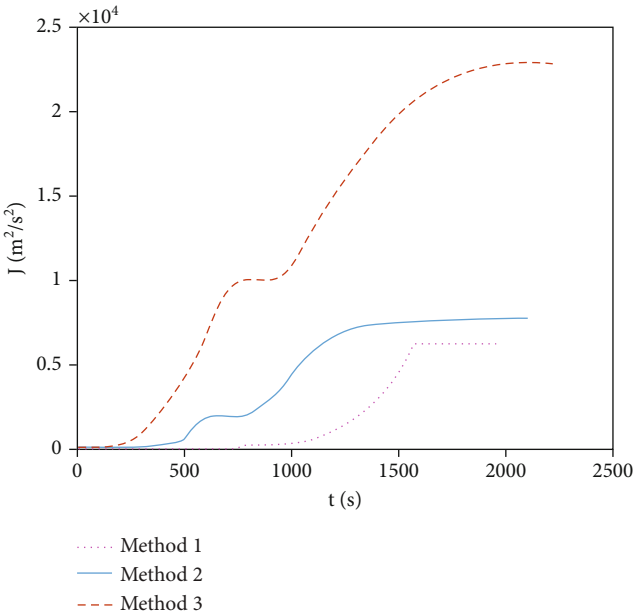

Figure 9: Comparison of performance indicators.

3.5. Trajectory Evaluation. The vehicle always performs significant lateral maneuvers to avoid no-fly zones which leads to consumption of energy. This paper takes the following total control effort performance index J into consideration for trajectory evaluation. Energy consumption index J reflects the maneuverability requirements of the vehicle, which is one of the necessary factors to be considered in engineering. The smaller the index J means the less energy consumption by the lateral maneuver and the better the trajectory performance. J is expressed as

$$J = \int a^2 dt = \int (L \sin \sigma)^2 dt \tag{52}$$

where a is the lateral acceleration related to control force and can be calculated by required centripetal force provided by the lateral component of lift.

3.6. The Process of Avoidance Strategy. For strategy of longitudinal motion, this paper suppresses errors in altitude and range by designing the angle of attack profile and online

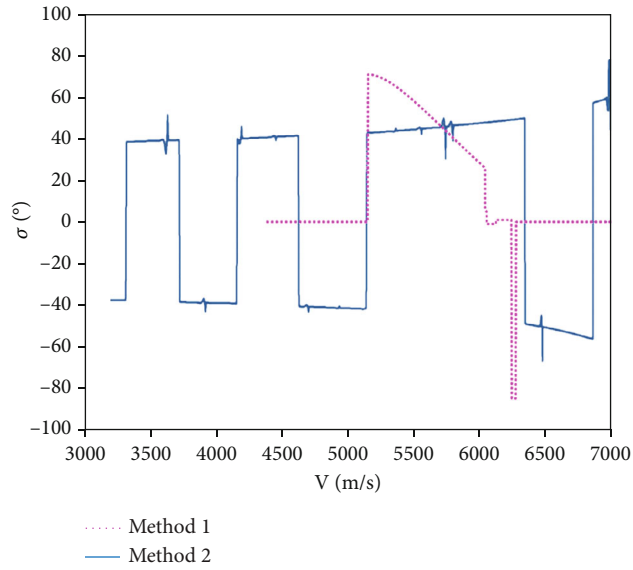

Figure 10: Comparison of bank angle-velocity curve.

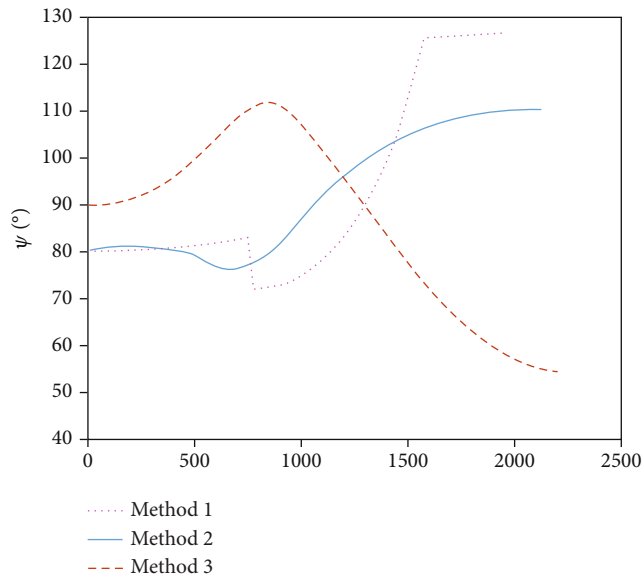

Figure 11: Comparison of heading angles.

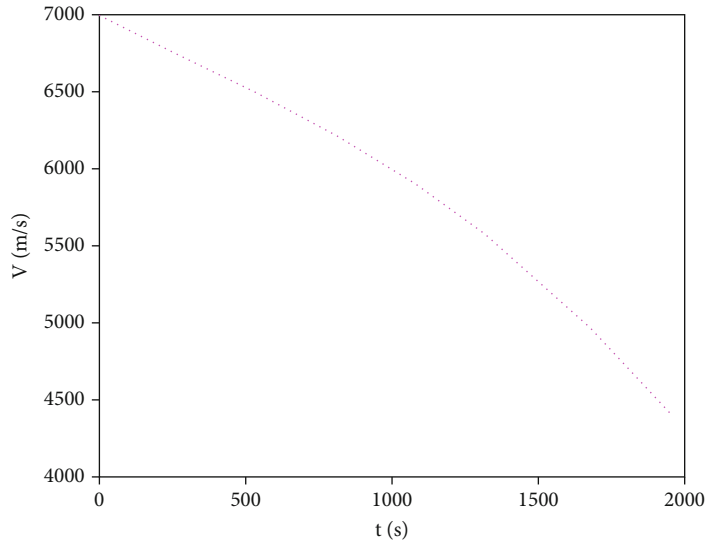

Figure 12: Velocity.

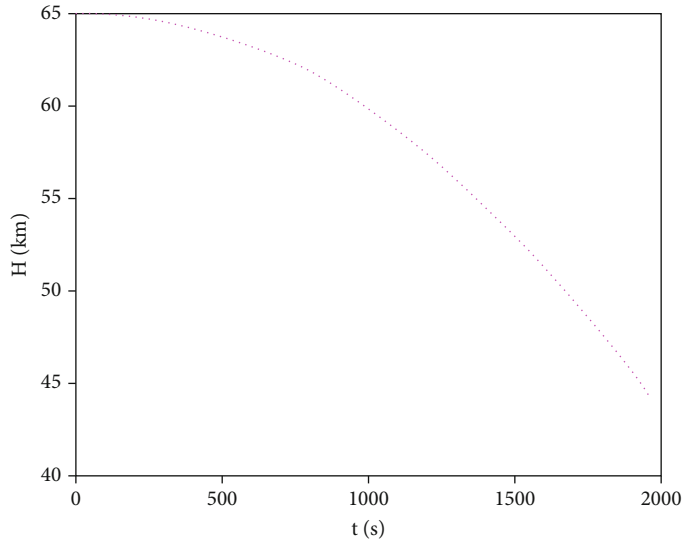

Figure 13: Height.

correction of range. For strategy of lateral motion, this paper addresses the avoidance problem through improved APFM. To overcome the shortcomings of APFM, repulsive force reconstruction is introduced to mitigate excessive maneuvering, and avoidance strategies based on minimum turning radius are employed to deal with mismatched magnitudes of forces. The flowchart of the proposed avoidance strategy is shown in Figure 7.

4. Simulation and Analysis

In this section, the proposed avoidance strategy is applied to solve numerical examples of complex distributed no-fly zone avoidance problem, which illustrates the effectiveness of the method.

4.1. Flight Mission. In simulation, the CAV-H model [28, 29] is used to verify the proposed method, whose mass and reference area are 907 kg and 0.4839 m^2, respectively. The vehicle achieves its maximum lift-to-drag ratio with the angle of attack being 10° and the maximal angle of attack being 25°. V_m and $V_{L/D}$ of the angle of attack profile in Equation (8) are set as 6000 m/s and 5000 m/s. Initial location of the vehicle is $(\lambda_0, \varphi_0) = (0°, 0°)$. The location of target is set as $(\lambda_T, \varphi_T) = (100°, 0°)$. The initial velocity of vehicle V_0 is 7000 m/s, and the terminal velocity V_f is no less than 3000 m/s. The vehicle's initial height H_0 is 65 km, and terminal height H_f should be more than 40 km. The initial heading angle ψ_0 and flight path angle θ_0 are given as 80° and 0°, respectively. The bank angle is constrained by $[-85°, 85°]$, and its maximum angular rate is 30°/s. The heading angle

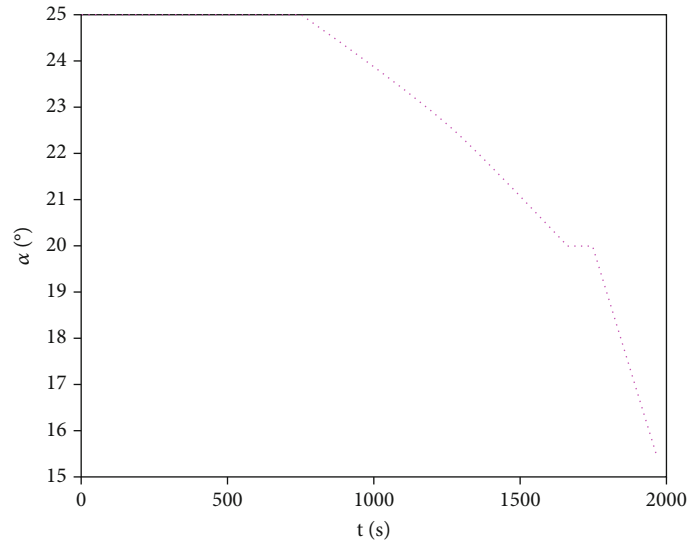

Figure 14: Attack angle.

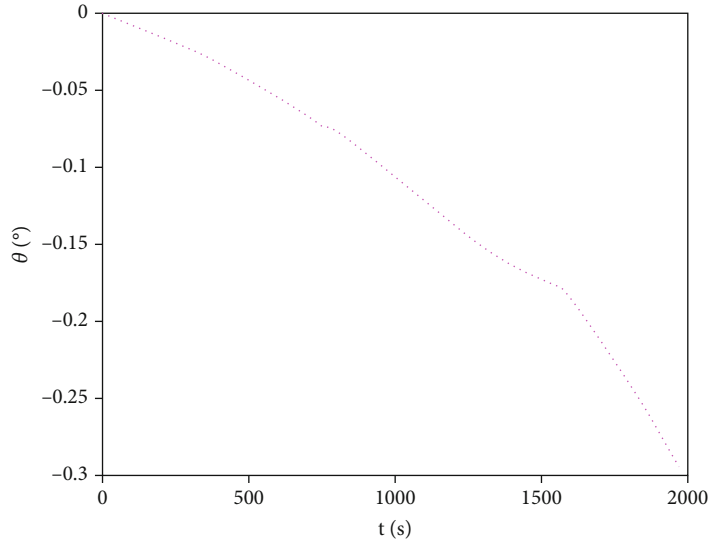

Figure 15: Flight path angle.

error threshold $\delta\psi$ is 5°. Path constraints are given as $q_{\max}$ = 200 kPa, $\dot{Q}_{\max}$ = 1000 kW/m^2, and $n_{\max}$ = 4.

The parameters of the proposed strategy are listed in Table 1, and the information of no-fly zones is shown in Table 2.

The parameters in Table 1 are determined through trial and error according to the scenario of the flight mission.

4.2. Trajectory Planning. To better illustrate the application effectiveness of the proposed method, a comparison is conducted by using multiple methods. Method 1 represents the method proposed in this paper. Method 2 refers to the dual-level path-trajectory generation method in reference [35]. Method 3 involves the Gaussian pseudospectral method, solved using the GPOPS toolbox in MATLAB.

The comparative simulation results of the three methods are shown in Figures 8–11, and Figures 12–15 show the simulation results of Method 1.

Figure 8 shows the comparison of trajectory ground track of the three methods, and it indicates that all three methods successfully avoid the no-fly zone. Method 3 has a different path direction compared to other methods, which is due to such method getting trapped in local optimum caused by the no-fly zones.

Figure 9 depicts the energy consumption index of the three methods. The index for Method 1 is 6183.42 m^2/s^2, Method 2 is 7764.61 m^2/s^2, and Method 3 is 23082.26 m^2/s^2. Therefore, the method proposed in this paper is better than other methods due to less energy consumption for lateral control.

Figure 10 depicts the bank angle command values of Method 1 and Method 2. From the bank angle-velocity

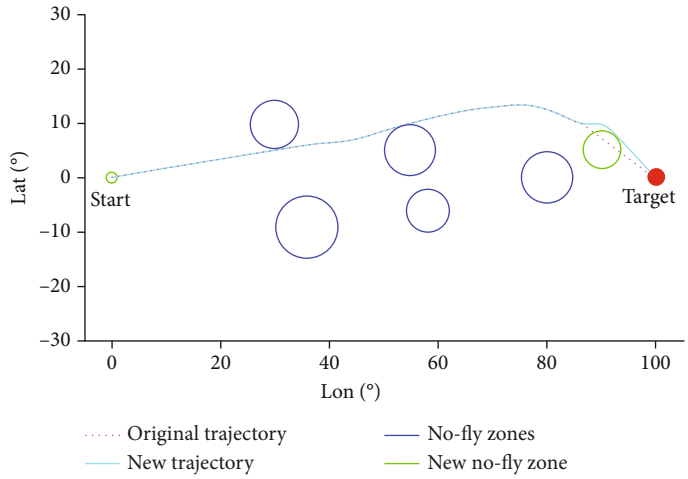

Figure 16: Comparison of ground track.

curve, it is evident that Method 2 maintains a relatively large bank angle for most of the flight. Method 1 avoids excessive maneuvering during flight, which results in generally smaller bank angles. Thus, by using Method 1, the energy consumption is lower, and the terminal velocity is larger than in Method 2.

Figure 11 depicts the comparison of heading angle. The changing trend of heading angle for Method 1 and Method 2 remains consistent, while Method 3 exhibits larger overall variations in heading angle. When using Method 1, there are sudden changes during the execution of the avoidance strategy based on minimum turning radius and during terminal guidance entry, while the heading angle remains stable during the rest of time.

From Figures 12 and 13, it can be seen that the velocity and height satisfy the terminal constraints, which means the vehicle has ability to execute subsequent missions after leaving no-fly zones.

Figures 14 and 15 indicate that the attack angle profile of the aircraft is reasonable, and the variation of speed and pitch angle during the flight is smooth.

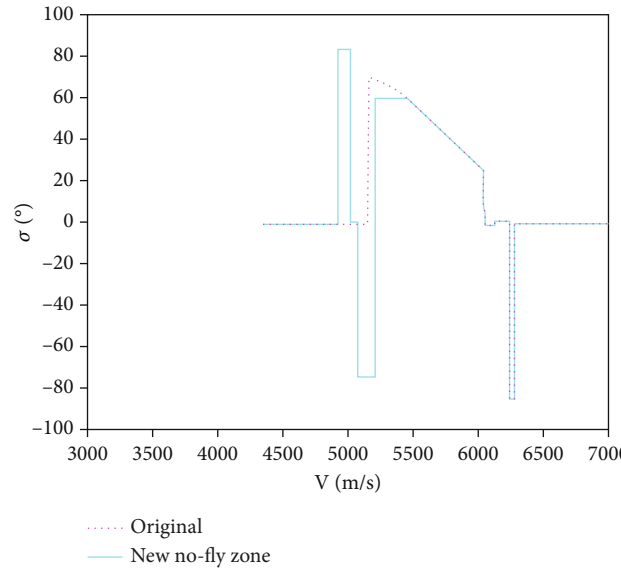

Figure 17: Comparison of bank angle-velocity curve.

4.3. Trajectory Planning With Sudden Threats

4.3.1. Static New No-Fly Zone. Assume that a new no-fly zone is discovered online with the center coordinates (90°, 5°) and a radius of 350 km at $t = 1400$ s. Simulation is carried out using the method proposed in this paper under the constraints of the new no-fly zone. The results are depicted in Figures 16 and 17.

According to the result of simulation, the aircraft's terminal height is 44.4 km, and its terminal velocity is 4350.83 m/s, satisfying the terminal constraints. Figure 15 shows the comparison of ground track between original constraints and constraints with static new no-fly zone. From Figure 15, it can be indicated that the aircraft successfully avoids the newly discovered no-fly zone and reaches the target.

Figure 16 displays the bank angle profile, and compared with the result without sudden threat, the vehicle makes larger maneuvering to avoid the new no-fly zone. It can be seen that the strategy proposed in this paper can be used for trajectory planning with sudden static threat, and the proposed method is highly applicable to cope with avoidance of changing no-fly zones.

4.3.2. Dynamic New No-Fly Zone. Assume that a new no-fly zone is discovered online with the center coordinates (90°, 5°) and a radius of 350 km at $t = 1400$ s. The new no-fly zone moves along the longitude direction with a speed of 5 m/s. Simulation calculations are conducted using the method proposed in this paper under the new constraints of the no-fly zones. The results of simulation are shown in Figures 18 and 19.

According to the result of simulation, the aircraft's terminal height is 44.3 km, and its terminal velocity is 4364.37 m/s, which satisfies the terminal constraints.

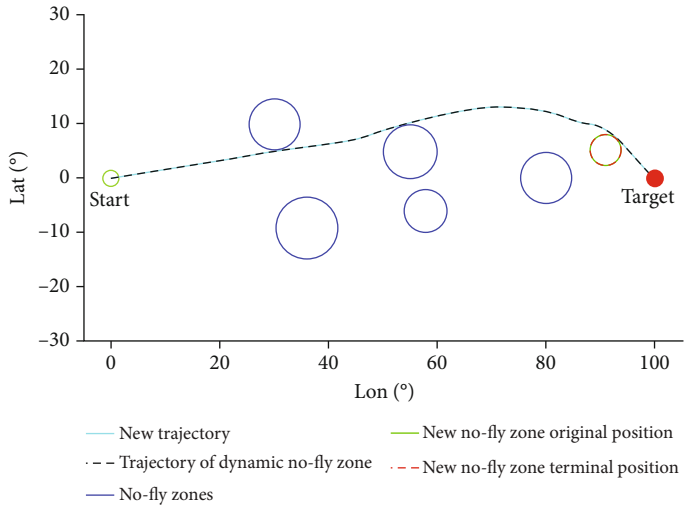

Figure 18: Comparison of ground track.

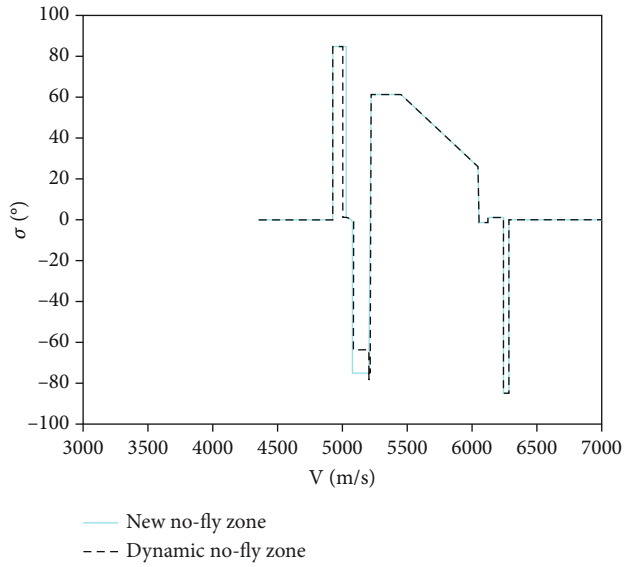

Figure 19: Comparison of bank angle-velocity curve.

Figure 18 depicts the comparison of ground track between constraints with static new no-fly zone and constraints with dynamic new no-fly zone. Trajectories in Figure 18 show the success of avoidance of dynamic no-fly zone, and the vehicle moves to target.

Figure 19 displays the bank angle profile of two conditions. When meeting dynamic threat, the vehicle makes different maneuvering to avoid comparing with static no-fly zone, and it can be seen that the method is sensitive to the moving of no-fly zones. The results of simulation indicate that the proposed strategy in this paper can be suitable for trajectory planning with sudden dynamic threat.

5. Conclusion

The paper proposes a novel strategy for complex distributed no-fly zone avoidance problems of hypersonic vehicle, which has the following characteristics:

1. When designing a strategy for lateral motion, an improved APFM is used in this paper which introduces improved attractive and repulsive potential fields, as well as velocity potential fields. By reconstructing repulsive force, the command bank angle is calculated, which effectively solves the problem of excessive maneuvering of traditional APFMs.

2. To cope with mismatched magnitudes of attractive and repulsive forces when vehicle is close to the obstacle, this paper presents an avoidance strategy based on the minimum turning radius, and the relationship between the aircraft's velocity direction, distance to the no-fly zone, no-fly zone radius, and command bank angle is derived. The command bank angle is updated during the avoidance of the no-fly zone according to the strategy, enabling successful avoidance.

Simulation results demonstrate the effectiveness of the proposed method. By using strategy in the paper, the vehicle is capable of avoiding complex no-fly zones with sudden threats. The simulation results show that the proposed strategy is an effective and feasible method to deal with complex distributed no-fly zone avoidance problems.

The strategy presented in this article provides an effective approach to solving the trajectory planning problem for high-speed aircraft in complex no-fly zones.

Data Availability Statement

Utilized data are cited in paper's references which also describe utilized algorithms.

Conflicts of Interest

The authors declare no conflicts of interest.

Funding

This work is supported in part by the National Natural Science Foundation of China (U21B2028) and the Hunan Province Graduate Innovation Funding Project (CX20230062).

References

[1] Q. Niu, Z. Yuan, B. Chen, and S. Dong, "Infrared radiation characteristics of a hypersonic vehicle under time-varying angles of attack," *Chinese Journal of Aeronautics*, vol. 32, no. 4, pp. 861–874, 2019.

[2] C. Bao, X. Zhou, P. Wang, R. He, and G. Tang, "A deep reinforcement learning-based approach to onboard trajectory generation for hypersonic vehicles," *Aeronautical Journal*, vol. 127, no. 1315, pp. 1638–1658, 2023.

[3] M. Zhang, Z. Chen, S. Wang, T. Chao, and M. Yang, *Reentry Trajectory Planning and Tracking Law of Hypersonic Glide Vehicle under the Influence of Environmental Uncertainty*, Springer Nature Singapore, Singapore, 2023.

[4] L. Mu, X. Wang, R. Xie, Y. Zhang, B. Li, and J. Wang, "A survey of the hypersonic flight vehicle and its guidance and control technology," *Journal of Harbin Institute of Technology*, vol. 51, no. 3, pp. 1–14, 2019.

[5] Z. Li, X. Yang, X. Sun, G. Liu, and C. Hu, "Improved artificial potential field based lateral entry guidance for waypoints passage and no-fly zones avoidance," *Aerospace Science and Technology*, vol. 86, pp. 119–131, 2019.

[6] Z. Liang, J. Long, S. Zhu, and R. Xu, "Entry guidance with terminal approach angle constraint," *Aerospace Science and Technology*, vol. 102, article 105876, 2020.

[7] T. R. Jorris and R. G. Cobb, "Three-dimensional trajectory optimization satisfying waypoint and no-fly zone constraints," *Journal of Guidance, Control, and Dynamics*, vol. 32, no. 2, pp. 551–572, 2009.

[8] W. Yu, W. Chen, Z. Jiang et al., "Analytical entry guidance for no-fly-zone avoidance," *Aerospace Science and Technology*, vol. 72, pp. 426–442, 2018.

[9] Z. Liu, J. Zhou, Z. Guo, J. Guo, and G. Wang, *Radau Pseudospectral Method-Based Cooperative Re-Entry Trajectory Optimization for Hypersonic Reentry Vehicle*, Springer Nature Singapore, Singapore, 2023.

[10] J. Wang, N. Cui, and C. Wei, "Rapid trajectory optimization for hypersonic entry using convex optimization and pseudospectral method," *Aircraft Engineering & Aerospace Technology*, vol. 91, no. 4, pp. 669–679, 2019.

[11] W. Fu, B. Wang, X. Li, L. Liu, and Y. Wang, "Ascent trajectory optimization for hypersonic vehicle based on improved chicken swarm optimization," *IEEE Access*, vol. 7, pp. 151836–151850, 2019.

[12] Y. Mao, D. Zhang, and L. Wang, "Reentry trajectory optimization for hypersonic vehicle based on improved Gauss pseudospectral method," *Soft Computing - A Fusion of Foundations, Methodologies & Applications*, vol. 21, no. 16, pp. 4583–4592, 2017.

[13] P. Pei, S. Fan, W. Wang, and D. Lin, "Online reentry trajectory optimization using modified sequential convex programming for hypersonic vehicle," *IEEE Access*, vol. 9, pp. 23511–23525, 2021.

[14] H. Zhang, H. Wang, N. Li, Y. Yu, Z. Su, and Y. Liu, "Time-optimal memetic whale optimization algorithm for hypersonic vehicle reentry trajectory optimization with no-fly zones," *Neural Computing and Applications*, vol. 32, no. 7, pp. 2735–2749, 2020.

[15] Y. Zhang, R. Zhang, and H. Li, "Graph-based path decision modeling for hypersonic vehicles with no-fly zone constraints," *Aerospace Science and Technology*, vol. 116, article 106857, 2021.

[16] Y. Zhang, R. Zhang, and H. Li, "Online path decision of no-fly zones avoidance for hypersonic vehicles based on a graph attention network," *IEEE Transactions on Aerospace and Electronic Systems*, vol. 59, no. 5, pp. 5554–5567, 2023.

[17] Z. Chen, H. Wang, S. Quan, and T. Chao, "Guidance algorithm for reentry vehicle considering target maneuvering and no-fly zone constraints," in *2021 40th Chinese Control Conference (CCC)*, Shanghai, China, 2021.

[18] R. Tian, Q. Zhang, L. Cui, and Y. Yu, "Avoidance of no-fly zone for hypersonic vehicle based on adaptice radau pseudospectral method," in *2022 7th International Conference on Intelligent Computing and Signal Processing (ICSP)*, Xi'an, China, 2022.

[19] Y. Ji, L. Ni, C. Zhao, C. Lei, and Y. Du, "TriPField: a 3D potential field model and its applications to local path planning of autonomous vehicles," *IEEE Transactions on Intelligent Transportation Systems*, vol. 24, no. 3, pp. 3541–3554, 2023.

[20] S. Sun, H. Guo, G. Wan, C. Dong, C. Zheng, and Y. Wang, "Coupled temporal variation information estimation and resolution enhancement for remote sensing spatial–temporal–spectral fusion," *IEEE Transactions on Geoscience and Remote Sensing*, vol. 61, pp. 1–18, 2023.

[21] A. Srivastava, V. R. Vasudevan, R. N. Harikesh, and P. B. Sujit, "A modified artificial potential field for UAV collision avoidance," in *2023 International Conference on Unmanned Aircraft Systems (ICUAS)*, Warsaw, Poland, 2023.

[22] M. Zhuang, G. Li, and K. Ding, "Obstacle avoidance path planning for apple picking robotic arm incorporating artificial potential field and a* algorithm," *IEEE Access*, vol. 11, pp. 100070–100082, 2023.

[23] J. Ren, K. A. McIsaac, R. V. Patel, and T. M. Peters, "A potential field model using generalized sigmoid functions," *IEEE Transactions on Systems, Man, and Cybernetics, Part B (Cybernetics)*, vol. 37, no. 2, pp. 477–484, 2007.

[24] M. Li, C. Zhou, L. Shao, H. Lei, and C. Luo, "An improved predictor-corrector guidance algorithm for reentry glide vehicle based on intelligent flight range prediction and adaptive crossrange corridor," *International Journal of Aerospace Engineering*, vol. 2022, Article ID 7313586, 18 pages, 2022.

[25] Y. Hu, C. Gao, J. Li, W. Jing, and W. Chen, "A novel adaptive lateral reentry guidance algorithm with complex distributed no-fly zones constraints," *Chinese Journal of Aeronautics*, vol. 35, no. 7, pp. 128–143, 2022.

[26] J. Hu, W. Sun, M. Zhang, T. Chao, and M. Yang, "Guidance method for re-entry glide vehicle considering no-fly zone avoidance," in *2023 42nd Chinese Control Conference (CCC)*, Tianjin, China, 2023.

[27] Z. Wang, S. Tang, and J. Guo, "Entry guidance command generation for hypersonic glide vehicles under threats and multiple constraints," *IEEE Access*, vol. 10, pp. 1–15, 2022.

[28] G. Richie, "The common aero vehicle - space delivery system of the future," in *Space Technology Conference and Exposition*, Albuquerque,NM,U.S.A., 1999.

[29] S. Walker and F. Rodgers, "Falcon hypersonic technology overview," in *AIAA/CIRA 13th International Space Planes*

and Hypersonics Systems and Technologies Conference, Capua, Italy, 2005.

[30] Y. Gao, G. Cai, X. Yang, and M. Hou, "Improved tentacle-based guidance for reentry gliding hypersonic vehicle with no-fly zone constraint," *IEEE Access*, vol. 7, pp. 119246–119258, 2019.

[31] H. Xu, G. Cai, and S. Zhang, "Modified aerodynamic coefficient fitting models of hypersonic gliding vehicle in reentry phase," *Journal of Astronautic*, vol. 42, no. 9, pp. 1139–1149, 2021.

[32] Y. Ren, J. Yang, and W. Xiong, "Hybrid guidance for common aero vehicle equilibrium glide reentry with multi-constraints," in *2019 IEEE International Conference on Unmanned Systems and Artificial Intelligence (ICUSAI)*, Xi'an, China, 2019.

[33] L. Pallottino, E. M. Feron, and A. Bicchi, "Conflict resolution problems for air traffic management systems solved with mixed integer programming," *IEEE Transactions on Intelligent Transportation Systems*, vol. 3, no. 1, pp. 3–11, 2002.

[34] P. Lu and S. Xue, "Rapid generation of accurate entry landing footprints," *Journal of Guidance, Control, and Dynamics*, vol. 33, no. 3, pp. 756–767, 2010.

[35] Y. Zhang, R. Zhang, and H. Li, "Dual-level path-trajectory generation with complex no-fly zone constraints for hypersonic vehicle," *Journal of Astronautics*, vol. 43, no. 5, pp. 615–627, 2022.